

Numerical Investigation of the Effects of Structural Property Variability on the Material Response of a Fibrous Ablator

Sean M. McDaniel* †, Rui Fu*, Adnan Taqi** Matthew J. Beck** and Alexandre Martin*

*Mechanical and Aerospace Engineering, University of Kentucky
151 Ralph G. Anderson Bldg. Lexington, Ky

**Chemical and Materials Engineering, University of Kentucky
177 F. Paul Anderson Tower Lexington, Ky

smmc255@g.uky.edu · rick.fu@uky.edu · adnan.taqi@uky.edu · m.beck@uky.edu · alexandre.martin@uky.edu

†Corresponding author

Abstract

Ablative materials are often used as thermal protection systems for spacecraft entering an atmosphere. One common material used in this application is a phenolic-impregnated carbon ablator (PICA), which is composed of carbon fibers surrounded by phenolic resin. Due to the orientation of these fibers, the material has large variations of mesoscale properties. This work explores the effects of using distributions of properties rather than effective properties. An orthotropic structural response solver is developed to calculate the displacement and stress field. This developed solver is coupled with an ablation response solver to investigate the effects of property variability applied on Young's Modulus on the stress field. This investigation leverages the boundary conditions and iso-Q geometry from ablation workshop test case 3.2 to examine these effects.

1. Introduction

Recent hypersonic atmospheric entry missions have used lightweight charring ablators as thermal protection systems (TPS). Phenolic Impregnated Carbon Ablator (PICA) is one such material that has been used as a TPS material for many missions including, Stardust,¹⁻⁴ MSL,^{5,6} and a similar material, PICA-X, is used by SpaceX for the Dragon spacecraft. Additionally, it is the planned material to be used for the forebody TPS on the entry vehicle for the Dragonfly mission to Titan.⁷ While PICA may appear homogeneous at a macroscale, the material is intrinsically inhomogeneous on the mesoscale. The construction of this material makes it so within small samples there is a large amount of variability in almost every property.⁸ This inhomogeneity means that any homogenized material properties input into a macroscale material response model are consequently "effective" properties. The use of these "effective" properties ignores the distribution of mesoscale properties within the bulk volume as well as the interactions between mesoscale regions of differing properties. Thereafter, there is a significant scatter of observed performance of TPS materials around model predictions, as mesoscale inhomogeneity leads to variability in observed behavior.⁸

Variability leads to unexpected system-level behavior, which necessitates the use of large factors of safety, thus increasing the cost and weight of the TPS. It is necessary to have a better understanding of the effects of this variability to be able to reduce the factors of safety while maintaining an acceptable level of risk and preventing system failure. Therefore, macroscale models must be updated to account for the local variations in material properties, which requires transitioning away from using "effective" material properties, and instead implementing a new process to apply distributions of properties. However, this endeavor introduces another obstacle as determining the quantitative values defining these distributions requires the development of a new set of tools.

Advances in micro Computed Tomography (CT)⁹⁻¹² have allowed unprecedented imaging of mesoscale volumes of disordered TPS materials. The recent development of PuMA^{13,14} has even allowed for analysis of computation of some properties of these microstructures. However, these efforts can and have only yielded a finite number of images of volumes of TPS materials. The characterization of the variations in material properties, and determining the quantitative relationships between local variations in structure on the scale of the size of fibers, requires the generation of orders of magnitude more samples than can reasonably be studied with micro-CT. To address this problem a code was developed to stochastically generate model Representative Volume Elements (mRVEs).¹⁵ These mRVEs are physically motivated computer-generated model volumes of fibrous carbon ablators constructed to reproduce the statistical range of geometries and configurations observed in real materials. The potential impact of mRVE generation lies in the

INVESTIGATION OF STRUCTURAL PROPERTY VARIABILITY IN A FIBROUS ABLATOR

ability to generate large numbers of unique mRVEs. Model RVEs reproduce the structural inhomogeneity of real TPS materials at the microscale using geometric primitives and statistical rules for their size and arrangement deduced from analyses of computed tomography reconstructions. The structures generated by this code can then be used to determine the distributions of properties that will then be sampled within the material response code.

The effects of the use of distributions of properties in material response codes have briefly been explored.¹⁶ However, this work assumed the material was isotropic and was limited to purely structural test cases. Additionally, distributions of properties using mRVE recreations of FiberForm have been calculated in,¹⁷ but these were calculated as a test of the methodology and an early version of the generation code was used.

This research presents two simultaneous threads of work. First, the calculation of distributions of structural properties using mRVEs. Secondly, it seeks to test the integration and ability to input distribution parameters and sample several distributions that are applied to multiple properties. As the primary focus of previous work has been on mechanical properties, this is a logical place to begin. This work explores the effects of applying distributions to Young's modulus, both In-Plane (IP) and Through-The-Thickness.

2. Methods

2.1 Structure Generation and Property Calculation

Both microstructure generation and property calculation are housed within the Kentucky Random Structure Toolkit (KRAStk), which is a Python interface that integrates in-house codes with various open-source geometry generation, meshing, and finite element packages. This toolkit seeks to capture the relevant geometric properties observed in the microstructure of the material. PICA uses FiberForm® as its substrate material, which is then infiltrated with phenolic resin. FiberForm is comprised of layers of carbon fibers held together by a carbonized organic binder. The orientation of these fibers is such that these materials exhibit transverse isotropic properties. The In-Plane (IP) fiber orientation is randomly distributed, and the Through-The-Thickness (TTT) orientation is such that the vast majority of the fibers fall within 15 degrees of the horizontal.¹⁰

These are the properties KRAStk seeks to capture as it generates mRVEs of these materials. FiberForm was decided to be the first fibrous carbon ablator to be added to the capabilities of KRAStk due to its close relationship with PICA and relative simplicity. To generate the FiberForm microstructure, cylindrical fibers are dropped in a box and allowed to settle under the influence of gravity. These fibers stack upon each other building up the microstructure as more and more fibers are placed. The mRVE of the desired dimension is then obtained by cutting it from the set of stacked fibers. The core details of this process are presented in greater detail in.¹⁵ The mRVEs are generated as plates to reduce both generation and property calculation time. To ensure there is no loss of accuracy the plates are made such that there is a sufficient number of geometric features in each direction. A recent update to the toolkit focused primarily on improving the mesh generation process. The mesh generation stage uses tetrahedra finite elements to conserve the topology of the mRVE and inserts additional tetrahedra at the fiber-fiber contacts to model the carbonized binder material.

The method proposed to predict the properties of nanoporous materials in¹⁸ is extended to predict the properties of fiber-based materials. The method is based on performing virtual experiments on the mRVEs using the Finite Element Method to compute the microscale elastic constants. These experiments assume the material is orthotropic and solve for the nine independent components of the stiffness tensor.

2.2 Numerical Framework

Both the solid mechanics and material response codes are contained within the framework of the Kentucky Aerothermodynamic and Thermal-response System (KATS).¹⁹ KATS has many capabilities, which include analyzing low-speed turbulent flows,²⁰ hypersonic flows,²¹ material response,¹⁹ solid mechanics, and thermo-mechanical coupling^{22,23} problems. Additionally, it includes a universal solver for modeling the interactions between fluid and solid.^{24,25} The efficiency of the computational performance is greatly increased due to KATS being designed for massively parallelized computations using ParMETIS²⁶ for domain decomposition and Open MPI²⁷ as the message passing interface.

2.3 Governing Equations

The structural response module in KATS is able to solve both transient and static problems.²³ For the present work, only the static solver is used. KATS structural response solves for the displacement field $\mathbf{u} \equiv (u_x, u_y, u_z)$. The evaluation

INVESTIGATION OF STRUCTURAL PROPERTY VARIABILITY IN A FIBROUS ABLATOR

of the structural response uses the governing equations for small elastic deformations, which are written as,

$$-\nabla \cdot \boldsymbol{\sigma} = \rho_s \mathbf{f}, \quad (1)$$

$$\boldsymbol{\sigma} = \mathbf{C}(\boldsymbol{\varepsilon} - \boldsymbol{\varepsilon}_T), \quad (2)$$

$$\boldsymbol{\varepsilon} = \frac{1}{2}[\nabla \mathbf{u} + (\nabla \mathbf{u})^T], \quad (3)$$

where $\boldsymbol{\sigma}$ is the first Piola-Kirchhoff stress tensor, ρ_s is the solid density, \mathbf{f} is the body force per unit mass, \mathbf{C} is the stiffness matrix and $\boldsymbol{\varepsilon}$ is the strain tensor. The temperature field obtained from the thermal response code is used to calculate the thermal strain, $\boldsymbol{\varepsilon}_T$, using

$$\boldsymbol{\varepsilon}_T = \boldsymbol{\alpha}(T - T_{ref}), \quad (4)$$

where the tensor $\boldsymbol{\alpha}$ is the coefficient of thermal expansion (CTE).

FiberForm is a transverse isotropic material meaning that it has differing properties in the IP and TTT directions. These directions may not be aligned with the Cartesian coordinate axes and there can be between one and three rotation angles between the orthotropic material axes and the Cartesian axes. For rotations about the x, y, and z axis using angles θ , ϕ , and γ (following the right-hand rule), respectively, the rotation matrices are

$$\mathbf{R}_x(\theta) = \begin{pmatrix} 1 & 0 & 0 \\ 0 & \cos \theta & -\sin \theta \\ 0 & \sin \theta & \cos \theta \end{pmatrix}, \quad (5)$$

$$\mathbf{R}_y(\phi) = \begin{pmatrix} \cos \phi & 0 & \sin \phi \\ 0 & 1 & 0 \\ -\sin \phi & 0 & \cos \phi \end{pmatrix}, \quad (6)$$

$$\mathbf{R}_z(\gamma) = \begin{pmatrix} \cos \gamma & -\sin \gamma & 0 \\ \sin \gamma & \cos \gamma & 0 \\ 0 & 0 & 1 \end{pmatrix}. \quad (7)$$

The overall rotation matrix is the product of each of the individual rotation matrices, as follows

$$\mathbf{R} = \mathbf{R}_x(\alpha)\mathbf{R}_y(\beta)\mathbf{R}_z(\gamma). \quad (8)$$

This rotation matrix can be used to go between the material and global coordinate systems for several properties, such as thermal conductivity (k), as follows,

$$\mathbf{k} = \begin{pmatrix} k_{xx} & k_{xy} & k_{xz} \\ k_{yx} & k_{yy} & k_{yz} \\ k_{zx} & k_{zy} & k_{zz} \end{pmatrix} = \mathbf{R} \begin{pmatrix} k_{IP} & & 0 \\ & k_{IP} & \\ 0 & & k_{TTT} \end{pmatrix} \mathbf{R}^T. \quad (9)$$

However, more work is necessary for the stiffness matrix, since in Voigt notation the stiffness matrix is a 6x6 representation of a rank 4 tensor.

$$\mathbf{Q} = \begin{pmatrix} R_{11}^2 & R_{12}^2 & R_{13}^2 & 2R_{12}R_{13} & 2R_{13}R_{11} & 2R_{11}R_{12} \\ R_{21}^2 & R_{22}^2 & R_{23}^2 & 2R_{22}R_{23} & 2R_{23}R_{21} & 2R_{21}R_{22} \\ R_{31}^2 & R_{32}^2 & R_{33}^2 & 2R_{32}R_{33} & 2R_{33}R_{31} & 2R_{31}R_{32} \\ R_{21}R_{31} & R_{22}R_{32} & R_{23}R_{33} & R_{22}R_{33} + R_{23}R_{32} & R_{21}R_{33} + R_{23}R_{31} & R_{22}R_{31} + R_{21}R_{32} \\ R_{31}R_{11} & R_{32}R_{12} & R_{33}R_{13} & R_{12}R_{33} + R_{13}R_{32} & R_{13}R_{31} + R_{11}R_{33} & R_{11}R_{32} + R_{12}R_{21} \\ R_{11}R_{21} & R_{12}R_{22} & R_{13}R_{23} & R_{12}R_{23} + R_{13}R_{22} & R_{13}R_{21} + R_{11}R_{23} & R_{11}R_{22} + R_{12}R_{21} \end{pmatrix} \quad (10)$$

This matrix can then be applied in a similar manner to the rotation matrix from before as shown,

$$\mathbf{C}' = \mathbf{Q}\mathbf{C}\mathbf{Q}^T. \quad (11)$$

INVESTIGATION OF STRUCTURAL PROPERTY VARIABILITY IN A FIBROUS ABLATOR

2.4 Material Variability

As previously discussed TPS material properties have a large amount of variation. In this study, this variability is addressed by sampling distributions to assign properties to each computational cell. The distribution of properties of the mRVEs were fit to a Gaussian distribution, which is sampled by KATS. The probability density function of a Gaussian distribution is given by

$$f(x|\mu, \sigma^2) = \frac{1}{\sqrt{2\pi\sigma^2}} e^{-\frac{(x-\mu)^2}{2\sigma^2}}, \quad (12)$$

where μ is the mean value and σ is the standard deviation. The results of sampling the distribution are applied to each cell and used to vary the property of interests about its mean value. An example of the results of this process is shown in Fig. 1 for Young's Modulus. This sampling is produced using the distribution parameters presented later in this work, which can be seen in Section 4 along with the results of the test case for which it was used.

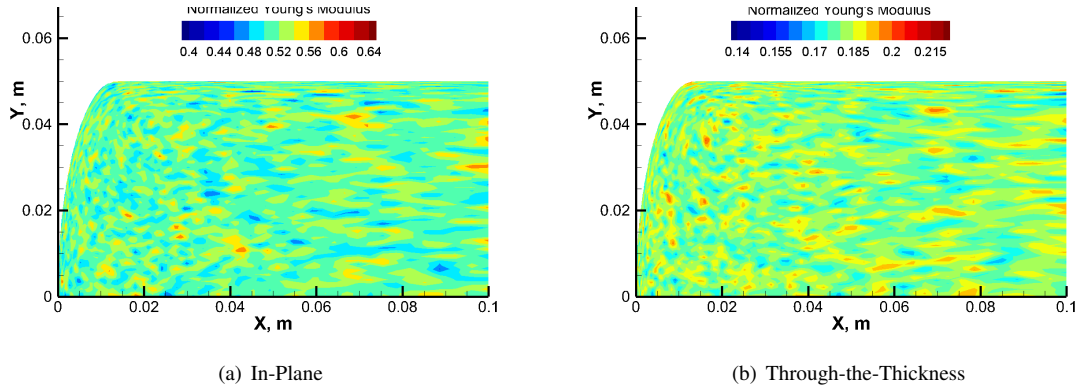


Figure 1: Normalized Young's Modulus

3. Verification of Orthotropic Module

In order to test that the orthotropic model was working as expected, a simple test case was developed and a code-to-code comparison was performed with Ansys[®] Workbench 2023 R1. The test case was created to test both the implementation of orthotropic stress calculation and the orthotropic thermal expansion. In this test case, the TTT direction is set to be aligned with the y -axis. The material properties are given in Table 1. The thermal boundary conditions were set so the

Table 1: Material Properties

E_{IP} (MPa)	E_{TTT} (MPa)	ν_{23}	ν_{13}	ν_{12}	μ_{IP} (MPa)	μ_{TTT} (MPa)	α_{IP} (K ⁻¹)	α_{IP} (K ⁻¹)
1	2	0.066	0.3	0.3	25.94	129.7	1×10^{-6}	2×10^{-6}

left face was held at 900 K and the right face was held at 300K. Both of these faces were fixed. All other surfaces were adiabatic and used frictionless support boundary conditions. To compare results the values were extracted along a path parallel to the x -axis and near the middle of the grid in the y -direction. These boundary conditions and the results path are shown in Fig. 2 along with the mesh used for KATS, which has dimensions of 120 by 120 cells.

Figure 3 shows the temperature, x -displacement, and Von Mises Stress along the path. The average relative error was calculated for each of these properties and is 0.002%, 0.582%, and 0.847%, respectively. These results show good agreement with Ansys and show that this new addition to KATS is ready to move forward to a full ablative test case with orthotropic properties.

4. Test Case Description

The test case performed in this work uses the theoretical ablative composite for open testing (TACOT) material. TACOT has properties based on PICA²⁸ and as such is classified as a light-weight carbon ablator though the material is theoretical. Each test case used the same iso-Q geometry, for which a description of the front surface can be found in.²⁹ Figure 4 displays the iso-Q sample geometry mesh that was used in this work.

INVESTIGATION OF STRUCTURAL PROPERTY VARIABILITY IN A FIBROUS ABLATOR

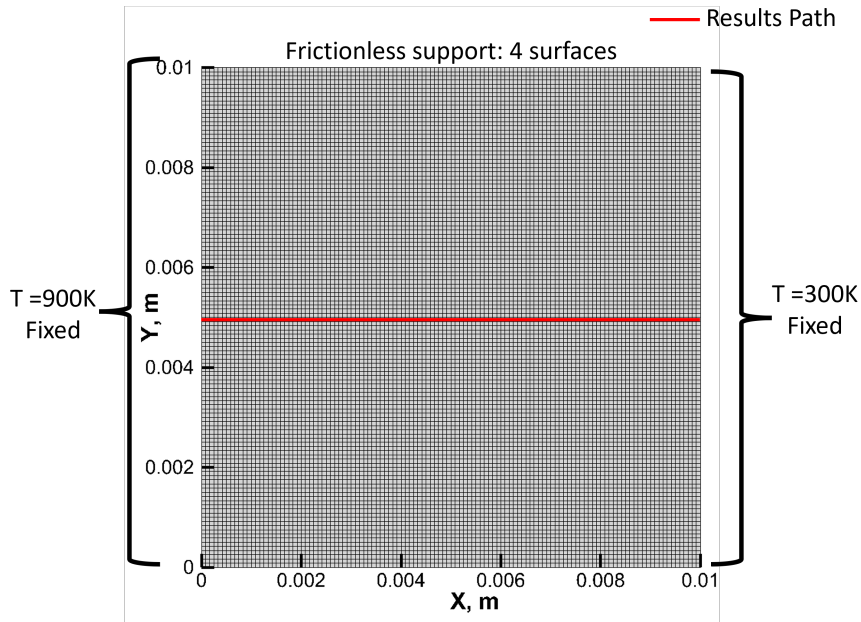


Figure 2: Boundary Conditions for 2D Thermal Expansion Case

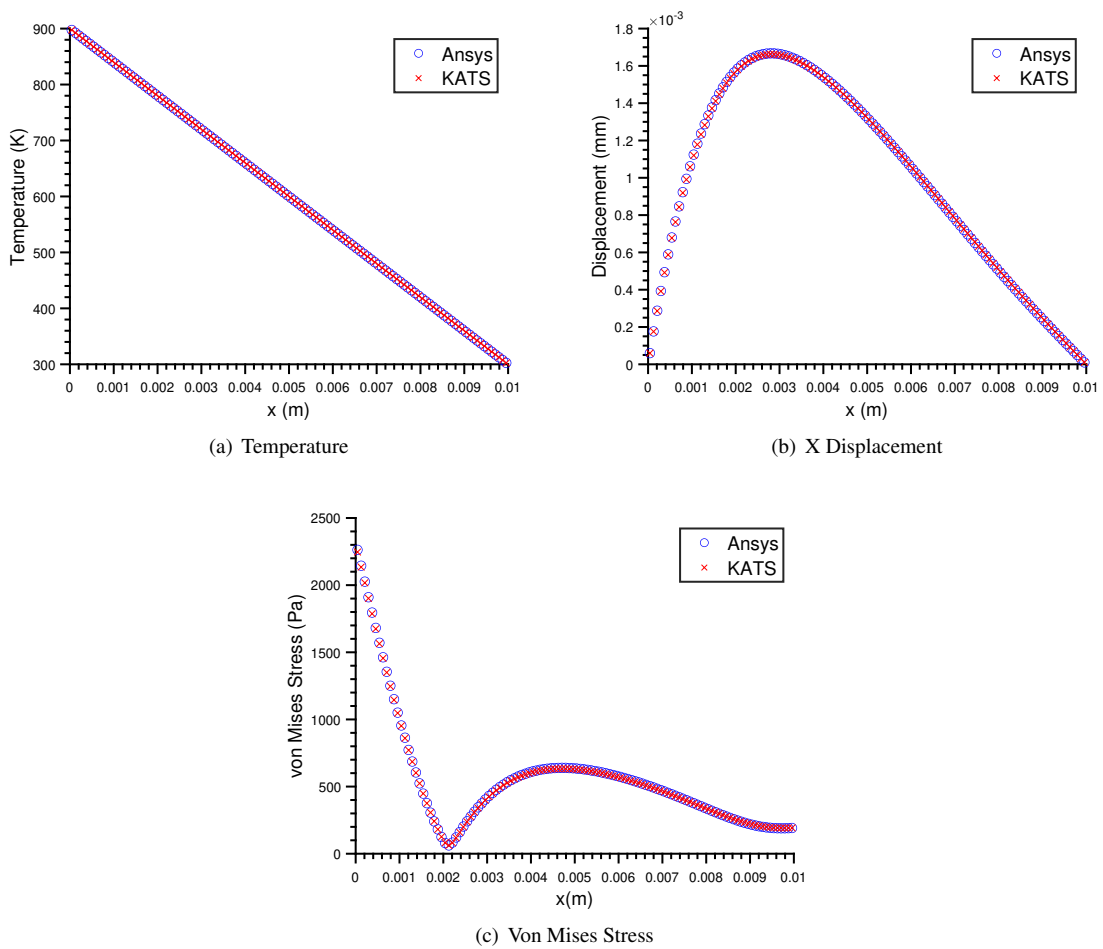


Figure 3: Results for thermal expansion case along path 1

INVESTIGATION OF STRUCTURAL PROPERTY VARIABILITY IN A FIBROUS ABLATOR

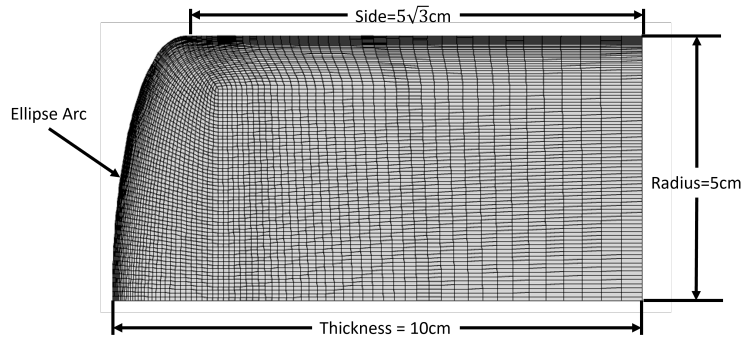
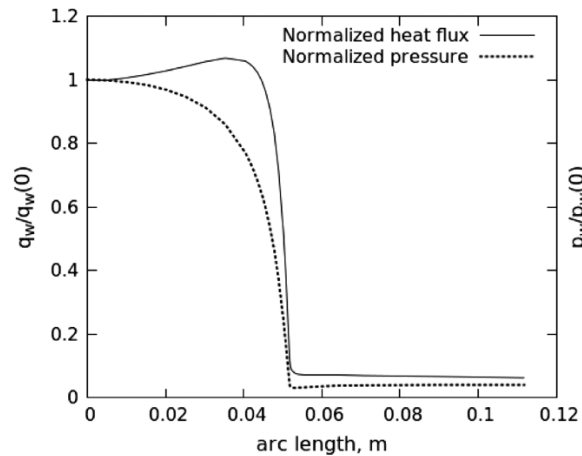


Figure 4: Iso-Q mesh

As the purpose of this work is to compare results with and without distributions of properties the boundary and initial conditions are identical for each test case. The sample is heated for 40 seconds. A uniform temperature ($T_0 = 300$ K) and pressure ($p_0 = 405.3$ Pa) are set as initial conditions. The time-dependent boundary-layer properties at the stagnation point are summarized in 2. The other boundary-layer assumption/properties along with the free stream conditions are omitted but can be found in.²⁹ For convenience, the heat flux and pressure profiles have been reproduced from²⁹ and may be seen in Fig. 5. In this work $q_w(0)$ was set to 2.55×10^6 W/m² and $\rho_e u_e C_h(0)$ was pre-multiplied with $q_w/q_w(0)$. The back side is set to be an adiabatic and impermeable wall. Since this material response solver is coupled

Table 2: Summary of environment properties adapted from²⁹

Time (s)	$\rho_e u_e C_h(0)$ (kg m ⁻² s ⁻¹)	h_e (J kg ⁻¹)	$p_w(0, t)$ (Pa)	$p_w(11.17, t)$ (Pa)
0	0.1×10^{-2}	0	405.3	405.3
0.1	0.1	2.5×10^7	10132.5	405.3
40	0.1	2.5×10^7	10132.5	405.3

Figure 5: Pressure and heat flux boundary condition reproduced from³⁰

with a solid mechanics solver for the stress it is crucial to also discuss the mechanical boundary conditions. The back wall is fixed and the front and side are free surfaces. One of the goals of this work is to test the newly implemented orthotropic model, therefore some IP properties were set to be nominally twice the value of the TTT property. These properties include both the CTE (α) and thermal conductivity (k). Several test cases were performed each using both different models and mechanical properties. In all cases, for simplification, the mechanical properties are set to be independent of temperature but are allowed to vary due to the transition from virgin to char as the material pyrolyzes. The char Young's modulus and CTE are one-tenth and one-hundredth of their respective virgin material values. The first case treats the material as isotropic using the average of the calculated Young's moduli in the IP direction (E_1 and

INVESTIGATION OF STRUCTURAL PROPERTY VARIABILITY IN A FIBROUS ABLATOR

E_2) from section 5.1. The average was taken here because the real materials are transverse isotropic so there is only one IP value. For this isotropic case, it is not necessary to use a value that is exact since it is only used for comparison to cases using the orthotropic stress calculation in terms of observed effects. That is to say the TTT Young's modulus could have been used instead and the values of stress would be reduced but the patterns of the stress field would remain the same. The second case is a fully transverse isotropic case with the IP Young's modulus being an average of the IP values in section 5.1 and TTT Young's modulus is the mean value for E_3 from that section. Both the IP CTE (α) and thermal conductivity (k) are set to be twice the nominal value. The third case is the same but the CTE is set so that IP and TTT are the same. The fourth case uses both IP CTE and thermal conduction at twice the nominal value but both IP and TTT directions use the IP value for Young's modulus. The fifth case is the same as case two but the variability is turned on using the distribution parameters in section 5.1 again with the IP value being averages for both the mean and standard deviations.

5. Results and Discussion

5.1 Property Distribution Calculation

The structural generation code (KRaSTk) was used to produce 100 mRVEs and calculate their properties. These structures were cut to be $140 \times 140 \times 20$ units with fibers that are 20 units long and have a radius of 1 unit. These dimensionless quantities can be converted to micrometers using the diameter of an individual fiber ($11 \mu\text{m}$). Then the mRVE's dimensions become $770 \times 770 \times 220 \mu\text{m}$. An example of a mRVE is provided in Fig. 6. The distributions and



Figure 6: Example Model Representative Volume Element

histograms of Young's modulus for each material direction are presented in Fig. 7. The data was then used to calculate

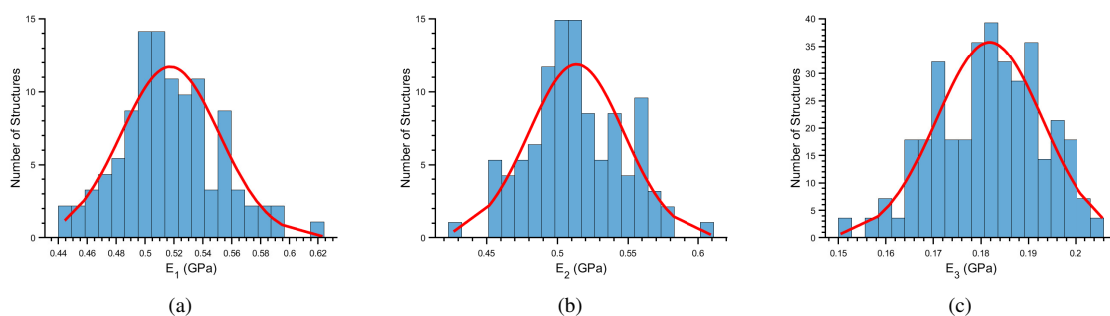


Figure 7: Distributions of mRVE Young's Moduli

the mean and standard deviation, to be used as distribution parameters in KATS, these values are given in Table 3.

These results show that key features of FiberForm are captured by the mRVEs. These features include transverse isotropy, shown by how similar the results are from the one and two directions. Additionally, real FiberForm also has a TTT Young's modulus that is significantly lower than its IP value. The magnitudes of these values seem quite high for FiberForm given that the best estimates found in literature have shown it on the order of KPa. This difference could be caused by using a value that is too large for the intrinsic Young's modulus of the fiber material. Additionally, the porosity of these structures was 79% whereas the real material has a porosity of around 87%. These two deviations are a clear indication that tweaks need to be made to the generation process. The ability to make these changes and see

INVESTIGATION OF STRUCTURAL PROPERTY VARIABILITY IN A FIBROUS ABLATOR

Table 3: Calculated Distribution Parameters

Property	μ (GPa)	σ (GPa)
E_1	0.517	0.034
E_2	0.513	0.035
E_3	0.181	0.011

how they affect property distributions is one of the major advantages of using mRVEs. It provides more insights into how features in the microstructure affect properties and could be leveraged to help design the next generation of TPS materials.

5.2 Iso-Q Test Case

5.2.1 Orthotropic Model

In this section, all results presented are taken at the end of the test case (40s). Before adding material variability into the model it is necessary to understand the effects of using an orthotropic stress calculation on the material response, which is the reason for running test cases one through four. The plots of temperature are the same for all cases within each model and are shown in Fig. 8 along with the differences between the two property models. It can be observed that the implemented orthotropic model predicts a higher front surface temperature. The region on the upper right shows a lower temperature distribution. These differences are caused by the difference in thermal conductivity.

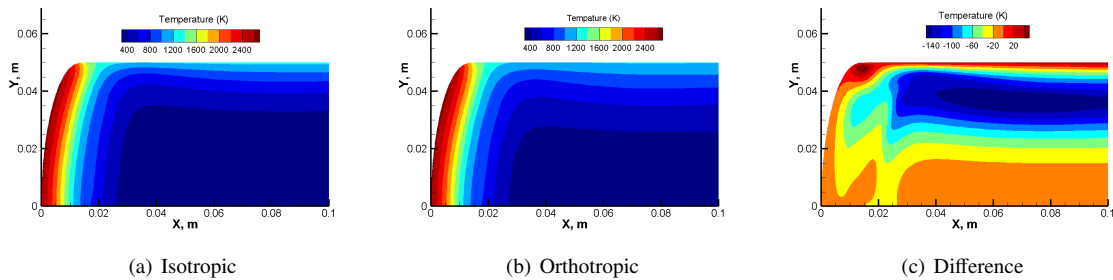


Figure 8: Temperature contour plots for iso-Q test cases

Figure 9 displays the total displacement field of four cases. It can be seen that the first case with an isotropic material shows the smallest thermal deformation. The absolute amount of the thermal expansion is in good agreement with the ref.²² The full orthotropic case predicts the largest thermal expansion - almost twice large compared to the isotropic one. It is interesting to see that thermal expansion has been doubled only because of the differences in the material directions. Additional two cases provide intermediate deformation levels with an isotropic CTE and Young's modulus. It can be seen that for these two cases, both the maximum level of displacement are lower than the full orthotropic model, while are larger than the isotropic case. This indicates that it is very important to model the TPS material as orthotropic since it will affect the structural response greatly.

To further compare each of these cases, results were extracted along three lines at $y = 1, 2.5,$ and 4 cm. The plots of displacement are shown in Fig. 10. These figures show that the displacement of the case using orthotropic stress calculation with fully transverse isotropic properties has by far the largest displacement. These lines of displacement paint a much clearer picture of the effects each case has on the results. Both the case with isotropic CTE and Young's modulus have an increase in displacement.

The amount the orthotropic stress calculation increased the displacement was initially surprising. However, when the other two cases using that model are examined it becomes clear that the combination of the two together amplifies the effects seen in each case. The most unexpected part was the effects on the Von Mises Stress, which are seen in 11. For the isotropic case, the thermal stress concentrates within the sample, which is at the pyrolysis front.²² After introducing the orthotropic model, the largest stress concentration moved to the front heating surface. Two additional cases, with either a constant CTE or Young's modulus, also deliver the same patterns.

Figure 12 shows a better comparison for the four cases presented previously. It can be seen that the isotropic case predicts the lowest stress level at all locations. After introducing the orthotropic, the stress level drastically increases - compared with the original one, the absolute level is almost 10 times larger in the fully orthotropic case. The results

INVESTIGATION OF STRUCTURAL PROPERTY VARIABILITY IN A FIBROUS ABLATOR

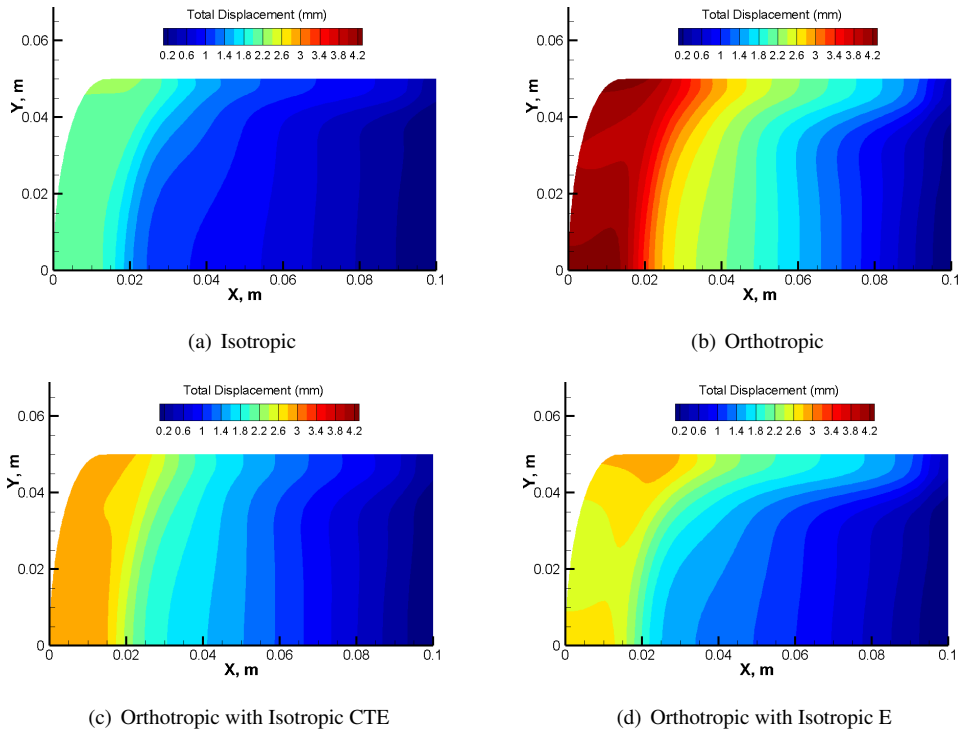


Figure 9: Displacement plots for iso-Q test cases

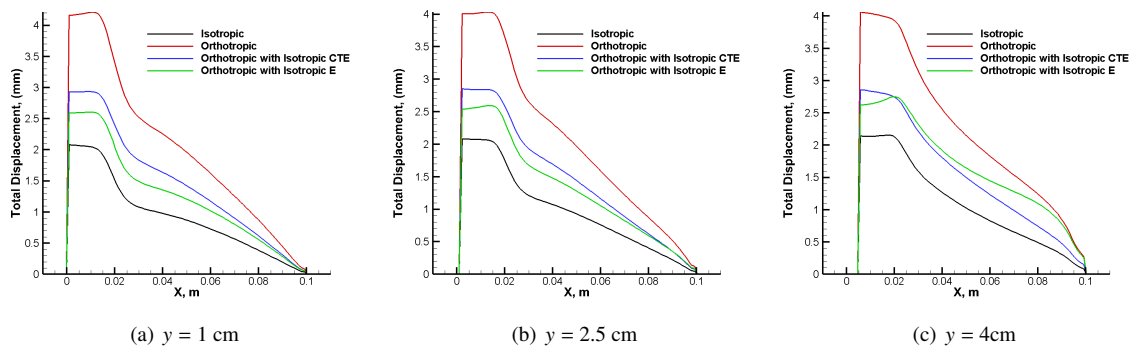


Figure 10: Displacement along three paths

indicate that the material orientations affect greatly the structural response, and the orthotropic model is necessary to accurately predict the thermo-mechanical performance of TPS materials.

5.2.2 Variability

Based on the previous test case it was determined that in order to see the effects of interest it was not necessary to run the test cases for the full 40s. Therefore the results in this section are taken at around 11s. Since, variability mainly effects the stress as it is applied only to Young's modulus only the Von Mises stress plots are presented in Fig. 13. This figure shows the scatter that variability brings to the stress. To see the effects of variability more clearly the Von Mises stress was normalized and the resulting histograms were plotted for the case using the fully transverse isotropic material with and without variability in Fig. 14. These results were plotted as the full iso-Q and then split into both virgin and char sections to show more clearly the effects. The virgin section does not show much difference between the case but this is because the virgin material has a large area that has little to no stress in it on one side and an region that has just reached the pyrolysis zone. The true effects of variability can be seen in the charge region. The majority of the stress overlap but in the case with variability there is more spread. This spread translates to tends to translate to more extreme value of stress.

INVESTIGATION OF STRUCTURAL PROPERTY VARIABILITY IN A FIBROUS ABLATOR

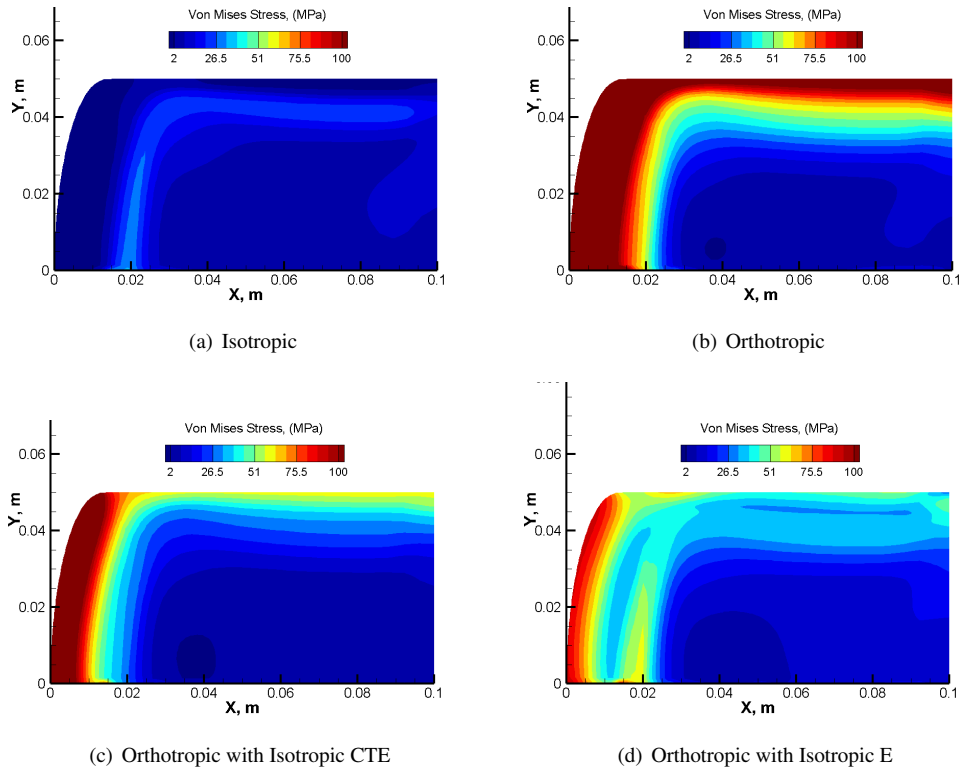


Figure 11: Von Mises stress plots for iso-Q test cases

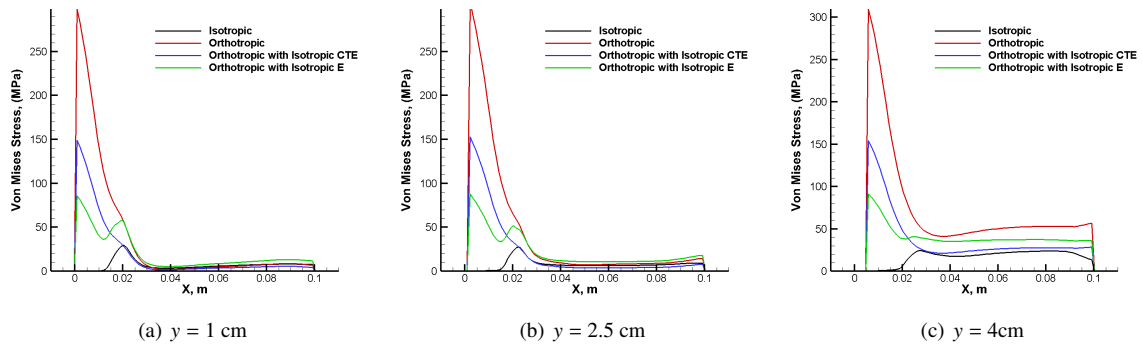


Figure 12: Von Mises stress along three paths

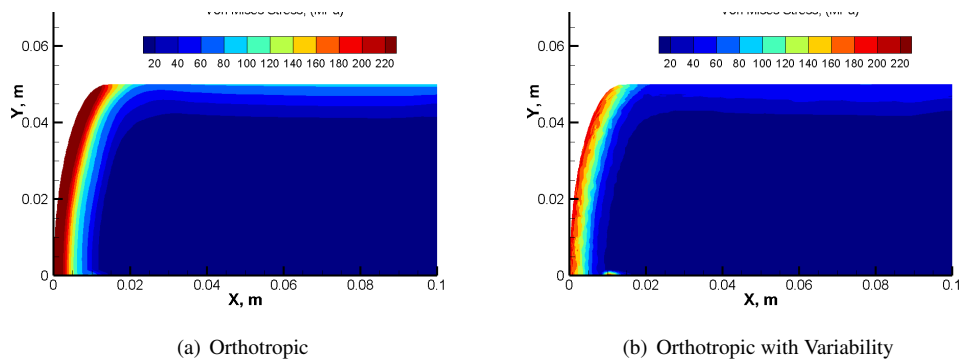


Figure 13: Von Mises stress plots for iso-Q test case with Variability

INVESTIGATION OF STRUCTURAL PROPERTY VARIABILITY IN A FIBROUS ABLATOR

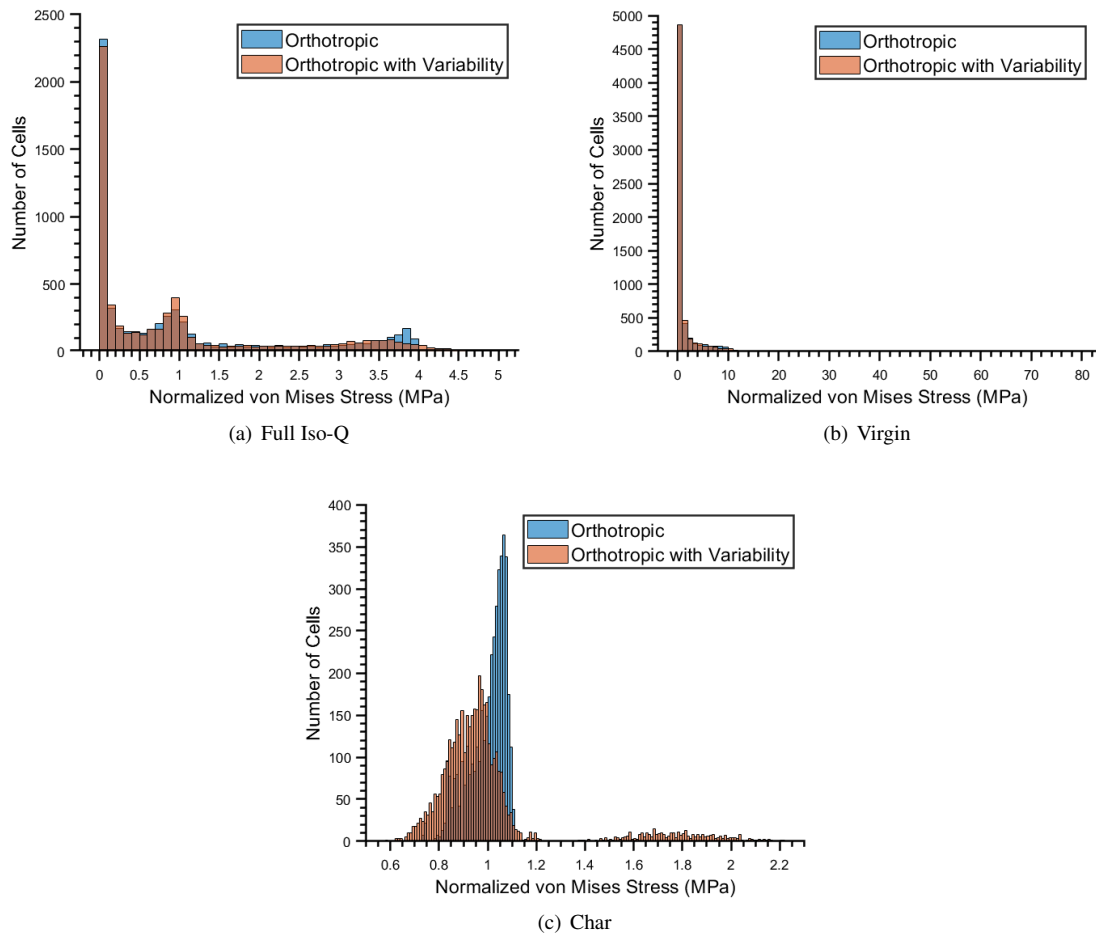


Figure 14: Histograms of Von Mises Stress

6. Conclusion and Outlook

This work has demonstrated a method for addressing variability in fibrous ablators. There were several unexpected findings that are still not fully understood, such as the mechanism that come together to generate the change in the pattern in the stress field. The complexity of the problem requires more advanced tools that have been explored so far. Some of these much need studies include both sensitivity analysis and uncertainty quantification. This work has built a framework understanding the effect of material variability. However, material variability cannot be separated for the size of the mRVEs used and this will need to be addressed in future work. Additionally, these tools will be used to examine the effects of defects in the material to better the predictive capabilities and reduce the risks in space travel.

Acknowledgments

The work presented here was supported by NASA ESI Award No. 80NSSC18K0261 (special thanks to M. Wright and M. Barnhardt (NASA Ames Research Center), as well as to T. Schwartzentruber (University of Minnesota)), by NASA Kentucky Space Grant Award No. NNX15AR69H, and by NASA STRI Award No. 80NSSC21K1117. The authors also thank the University of Kentucky Center for Computational Sciences and Information Technology Services Research Computing for their aid and use of the Lipscomb Compute Cluster and associated research computing resources. Additionally, a special thanks to Mujan Seif (University of Kentucky) for her guidance and support in completing this project.

References

- [1] D. A. Kontinos and M. J. Wright. Introduction: Atmospheric entry of the stardust sample return capsule. *Journal of Spacecraft and Rockets*, 47(5) pages 705–707, 2010. DOI [10.2514/1.51522](https://doi.org/10.2514/1.51522).
- [2] K. A. Trumble, I. Cozmuta, S. Sepka, P. Jenniskens, and M. Winter. Postflight aerothermal analysis of the stardust sample return capsule. *Journal of Spacecraft and Rockets*, 47(5) pages 765–774, 2010. DOI [10.2514/1.41514](https://doi.org/10.2514/1.41514).
- [3] M. W. Winter and K. A. Trumble. Near-ultraviolet emission spectroscopy during an airborne observation of the stardust reentry. *Journal of Spacecraft and Rockets*, 48(1) pages 59–71, 2011. DOI [10.2514/1.38176](https://doi.org/10.2514/1.38176).
- [4] A. Martin and I. D. Boyd. Modeling of heat transfer attenuation by ablative gases during the stardust reentry. *Journal of Thermophysics and Heat Transfer*, 29(3) pages 450–466, 2015. DOI [10.2514/1.T4202](https://doi.org/10.2514/1.T4202).
- [5] D. Bose, T. White, M. Mahzari, and K. Edquist. Reconstruction of aerothermal environment and heat shield response of mars science laboratory. *Journal of Spacecraft and Rockets*, 51(4) pages 1174–1184, 2014. DOI [10.2514/1.A32783](https://doi.org/10.2514/1.A32783).
- [6] T. Lincoln. Seeing red. *Nature*, 479(7374) pages 446–446, November 2011. DOI [10.1038/479446a](https://doi.org/10.1038/479446a).
- [7] A. Brandis, D. Saunders, G. Allen, E. Stern, M. Wright, M. Mahzari, C. Johnston, J. Hill, D. Adams, and R. Lorenz. Aerothermodynamics for dragonfly’s titan entry. *International Planetary Probe Workshop*, 2018.
- [8] F. Panerai, J. D. White, T. J. Cochell, O. M. Schroeder, N. N. Mansour, M. J. Wright, and A. Martin. Experimental measurements of the permeability of fibrous carbon at high-temperature. *International Journal of Heat and Mass Transfer*, v.101 pages 267–273, 2016. DOI [10.1016/j.ijheatmasstransfer.2016.05.016](https://doi.org/10.1016/j.ijheatmasstransfer.2016.05.016).
- [9] J. C. Ferguson, F. Panerai, J. Lachaud, A. Martin, S. C. Bailey, and N. N. Mansour. Modeling the oxidation of low-density carbon fiber material based on micro-tomography. *Carbon*, v.96 pages 57–65, 2016. DOI [10.1016/j.carbon.2015.08.113](https://doi.org/10.1016/j.carbon.2015.08.113).
- [10] F. Panerai, J. C. Ferguson, J. Lachaud, A. Martin, M. J. Gasch, and N. N. Mansour. Micro-tomography based analysis of thermal conductivity, diffusivity and oxidation behavior of rigid and flexible fibrous insulators. *International Journal of Heat and Mass Transfer*, v.108 pages 801–811, 2017. DOI [10.1016/j.ijheatmasstransfer.2016.12.048](https://doi.org/10.1016/j.ijheatmasstransfer.2016.12.048).
- [11] M. F. Ho, S. Leclaire, J.-Y. Trépanier, M. Reggio, and A. Martin. Permeability through fibrous thermal insulators with the lattice boltzmann method. *International Journal of Heat and Mass Transfer*, 2020. DOI [10.2514/1.T6154](https://doi.org/10.2514/1.T6154).
- [12] R. Jambunathan, D. Levin, A. Borner, J. Ferguson, and F. Panerai. Prediction of gas transport properties through fibrous carbon preform microstructures using direct simulation monte carlo. *International Journal of Heat and Mass Transfer*, v.130 pages 923–937, 2019. DOI [10.1016/j.ijheatmasstransfer.2018.11.006](https://doi.org/10.1016/j.ijheatmasstransfer.2018.11.006).
- [13] J. C. Ferguson, F. Panerai, A. Borner, and N. N. Mansour. PuMA: The porous microstructure analysis software. *SoftwareX*, v.7 pages 81–87, 2018. DOI [10.1016/j.softx.2018.03.001](https://doi.org/10.1016/j.softx.2018.03.001).
- [14] J. C. Ferguson, F. Semeraro, J. M. Thornton, F. Panerai, A. Borner, and N. N. Mansour. Update 3.0 to PuMA: The porous microstructure analysis software. *SoftwareX*, v.15 page 100775, 2021. DOI [10.1016/j.softx.2021.100775](https://doi.org/10.1016/j.softx.2021.100775).
- [15] S. McDaniel, M. Seif, R. Fu, M. Beck, and A. Martin. Development of stochastic model for fibrous ablators. In *AIAA Scitech 2021 Forum*, page 1473, 2021. DOI [10.2514/6.2021-1473](https://doi.org/10.2514/6.2021-1473).
- [16] R. Fu, S. McDaniel, M. Beck, and A. Martin. Numerical study of material uncertainties in thermal and structural responses in charring ablation. In *AIAA Scitech 2020 Forum*, page 0256, 2020. DOI [10.2514/6.2020-0256](https://doi.org/10.2514/6.2020-0256).
- [17] M. Seif, S. McDaniel, M. Beck, and A. Martin. Stochastic modeling of elastic behavior of fibrous ablators. In *AIAA Scitech 2021 Forum*, page 1585, 2021. DOI [10.2514/6.2021-1585](https://doi.org/10.2514/6.2021-1585).
- [18] M. N. Seif, D. J. Richardson, K. M. Moody, M. Martin, M. Turner, S. W. Mays, T. J. Balk, and M. J. Beck. Stochastic approach for determining properties of randomly structured materials: Effects of network connectivity. *Acta Materialia*, v.222 page 117382, 2022. DOI [10.1016/j.actamat.2021.117382](https://doi.org/10.1016/j.actamat.2021.117382).

INVESTIGATION OF STRUCTURAL PROPERTY VARIABILITY IN A FIBROUS ABLATOR

- [19] H. Weng, S. C. C. Bailey, and A. Martin. Numerical study of iso-Q sample geometric effects on charring ablative materials. *International Journal of Heat and Mass Transfer*, v.80 pages 570–596, 2015. DOI [10.1016/j.ijheatmasstransfer.2014.09.040](https://doi.org/10.1016/j.ijheatmasstransfer.2014.09.040).
- [20] Z. Li, H. Zhang, S. C. C. Bailey, J. B. Hoagg, and A. Martin. A data-driven adaptive Reynolds-averaged Navier-Stokes $k-\omega$ model for turbulent flow. *Journal of Computational Physics*, v.345 pages 111–131, 2017. DOI [10.1016/j.jcp.2017.05.009](https://doi.org/10.1016/j.jcp.2017.05.009).
- [21] H. Zhang. *High Temperature Flow Solver For Aerothermodynamics Problems*. Ph.d. thesis, University of Kentucky, Lexington, KY, July 2015. Online at <http://uknowledge.uky.edu/me/etds/64>.
- [22] R. Fu, H. Weng, J. F. Wenk, and A. Martin. Thermomechanical Coupling for Charring Ablators. *Journal of Thermophysics and Heat Transfer*, v.32 pages 369–379, Oct 2018. DOI [10.2514/1.T5194](https://doi.org/10.2514/1.T5194).
- [23] R. Fu, H. Weng, J. F. Wenk, and A. Martin. Thermal Expansion for Charring Ablative Materials. *Journal of Thermophysics and Heat Transfer*, v.52 pages 1–9, June 2019. DOI [10.2514/1.t5718](https://doi.org/10.2514/1.t5718).
- [24] R. Fu and A. Martin. Hinge method for immersed boundary problems and micro-scale carbon fiber material response. In *AIAA Scitech 2020 Forum*, AIAA Paper 2021-0482, 2020. DOI [10.2514/6.2020-0482](https://doi.org/10.2514/6.2020-0482).
- [25] R. Fu and A. Martin. Hinge method for cfd and fluid-ablation interaction modeling. In *AIAA Aviation 2021 Forum*, AIAA Paper 2021-3132, Virtual Event, August 2021. DOI [10.2514/6.2021-3132](https://doi.org/10.2514/6.2021-3132).
- [26] K. Schloegel, G. Karypis, and V. Kumar. Parallel multilevel algorithms for multi-constraint graph partitioning. In *Euro-Par*, pages 296–310. Springer, 2000. DOI [10.1007/3-540-44520-X_39](https://doi.org/10.1007/3-540-44520-X_39).
- [27] E. Gabriel, G. E. Fagg, G. Bosilca, T. Angskun, J. J. Dongarra, J. M. Squyres, V. Sahay, P. Kambadur, B. Barrett, A. Lumsdaine, R. H. Castain, D. J. Daniel, R. L. Graham, and T. S. Woodall. Open MPI: Goals, concept, and design of a next generation MPI implementation. In *Proceedings, 11th European PVM/MPI Users' Group Meeting*, pages 97–104, Budapest, Hungary, September 2004.
- [28] J. Lachaud, A. Martin, I. Cozmuta, and B. Laub. Ablation test-case series 1. *4th AFOSR/SNL/NASA Ablation Workshop*, 2010. DOI [10.13023/ablation.test.01](https://doi.org/10.13023/ablation.test.01).
- [29] T. van Eekelen, A. Martin, J. Lachaud, and D. Bianchi. Ablation test-case series 3: Numerical simulation of ablative-material response: Code and model comparisons. *6th Ablation Workshop*, 2014. Online at https://uknowledge.uky.edu/me_facpub/20.
- [30] H. Weng and A. Martin. Numerical investigation of thermal response using orthotropic charring ablative material. *Journal of Thermophysics and Heat Transfer*, 29(3) pages 429–438, 2015. DOI [10.2514/1.T4576](https://doi.org/10.2514/1.T4576).